

SUPPORTING INFORMATION

for

Topological Stone-Wales Defects Enhance Bonding and Electronic Coupling at the Graphene/Metal Interface

Benedikt P. Klein^{1,2,5}, Alexander Ihle³, Stefan R. Kachel¹, Lukas Ruppenthal¹, Samuel J. Hall^{4,5},
Lars E. Sattler⁶, Sebastian M. Weber⁶, Jan Herritsch¹, Andrea Jaegermann¹, Daniel Ebeling³,
Reinhard J. Maurer⁵, Gerhard Hilt⁶, Ralf Tonner-Zech^{1†}, André Schirmeisen^{3*},
J. Michael Gottfried^{1*}

¹*Fachbereich Chemie, Philipps-Universität Marburg, Hans-Meerwein-Straße. 4,
35032 Marburg, Germany*

²*Diamond Light Source, Harwell Science and Innovation Campus,
Didcot, OX11 0DE, United Kingdom*

³*Institut für Angewandte Physik, Justus-Liebig-Universität Gießen,
Heinrich-Buff-Ring 16, 35392 Gießen, Germany*

⁴*MAS Centre for Doctoral Training, Senate House, and* ⁵*Department of Chemistry, University of
Warwick, Gibbet Hill Road, Coventry, CV4 7AL, United Kingdom*

⁶*Institut für Chemie, Carl von Ossietzky Universität Oldenburg,
Carl-von-Ossietzky-Straße. 9-11, 26111 Oldenburg, Germany*

[†]*Current address: Wilhelm-Ostwald-Institut für Physikalische und Theoretische Chemie,
Universität Leipzig, Linnéstraße 2, 04103 Leipzig, Germany*

1. Supplementary Methods

1.1 Density Functional Theory Calculations.

The basic calculations for the adsorbed molecules were performed using the Vienna Ab Initio Simulation Package (VASP)¹⁻⁴ with the generalized gradient approximation (GGA) proposed by Perdew, Burke, and Ernzerhof (PBE)⁵ for the exchange-correlation functional in combination with the D3 van-der-Waals correction scheme with Becke-Johnson damping,⁶⁻⁷ and the projector-augmented wave (PAW) ansatz⁸⁻⁹ for the atomic cores. A plane-wave cutoff energy of 350 eV, a vacuum layer of 30 Å and a 6×6×1 Monkhorst Pack k-point grid were chosen.

X-ray absorption spectra were calculated using the pseudopotential plane-wave code CASTEP-18.1,¹⁰ using the PBE functional with a plane-wave cutoff of 450 eV and an 8×8×1 k-point grid. For the XPS shifts the delta self-consistent field (Δ SCF) method of constraining electronic occupations to resemble full core-hole excitations was used. NEXAFS spectra were simulated using on-the-fly generated USPPs and the CASTEP module ELNES¹¹ and the transition-potential approach.¹²⁻¹³ This method constrains the occupation of the initial state orbital, of the C1s, to 0.5 and the corresponding Kohn-Sham eigenenergies are taken to reflect the NEXAFS spectrum. Individual XAS calculations for each carbon atom allow for an atom-wise projected NEXAFS spectrum to be generated. MO projections and core-level spectra were processed using a self-written post-processing tool for CASTEP.¹⁴ The intensities of the MO contributions for the adsorbed molecules were scaled by a constant factor to enable a better comparison. The absolute values for those intensities are much reduced compared to the free molecules due to the presence of a large number of metal states.

The pEDA method¹⁵ allows to decompose the bond energy into several physically well-defined terms, thus permitting a more detailed interpretation of the character of the chemical bond between two fragments.¹⁶ In our case the fragments are chosen to be the molecule and the surface in their respective singlet electronic states.

The calculations for the free graphene defect structures were also performed in VASP on the level PBE-D3(BJ)/PAW with a plane-wave cutoff energy of 350 eV and 30 Å vacuum, the k-grid consisted only of the Γ -point. The unit cell with 456 carbon atoms was chosen large enough to contain one Stone-Wales defect or two 5-7 defects isolated by a sufficiently large distance. The adsorbed graphene structures were generated with a 4-layer Cu slab and 10 Å vacuum layer. The structures contain 912 copper atoms and 456 carbon atoms and are based on the simple (1×1) adsorption structure of the ideal graphene on Cu(111) often found in the literature¹⁷ The lattice mismatch between the optimized cell geometry of free-standing graphene and the forced (1×1) superstructure is only about 2% in the DFT-optimized lattice parameters. The optimization of the adsorbate structure was performed in a multistep procedure: After preoptimization steps with

reduced parameters (number of Cu-layers, plane-wave cutoff), the final optimization was performed with of 350 eV cutoff and four Cu-layers, the lower two of which were kept fixed.

2. Supplementary Discussion

2.1 Supplementary nc-AFM Discussion

To reveal adsorption positions of the molecules with regard to the Cu(111) lattice, the adjacent Cu surface has been scanned with atomic resolution (Supplementary Fig. 2a,b).¹⁸ Fig. S2c and S2d show corresponding AFM images with fitted molecular structures (red and black structures) and substrate lattices (blue dots indicate Cu(111) top sites). While pyrene is adsorbed with its long axis parallel to a $\langle 1-21 \rangle$ symmetrical crystallographic direction (see white arrows in Fig. S2c,d) azupyrene is rotated by about 19° with respect to this direction. The pyrene molecule can be fitted by two molecular structures that either match with the left part of the molecule (red structure in Fig. S2c,e) or with the rightmost ring (black structure in Fig. S2c,e). The red and black structures are shifted by approximately 140 pm along the $[1-21]$ direction and correspond to adsorption of the carbon rings above hcp and fcc hollow sites, respectively (see Fig. S2). Our DFT calculations reveal that these are the two most favorable adsorption positions of pyrene on Cu(111), which differ by about 10 meV (~ 1 kJ/mol) in adsorption energy. From this analysis, we can rationalize that the pyrene molecule is manipulated by the CO tip during scanning, which indicates a relatively weak molecule-substrate interaction. We have recently uncovered similar non-stationary adsorption structures for 4,4''-diamino-p-terphenyl and 4-bromo-3''-iodo-p-terphenyl on Cu(111).¹⁹⁻²⁰

The constant-height AFM images of azupyrene (Fig. 3a) and pyrene (Fig. 3b) in the main text confirm the different topologies of the ring systems: 5-7-5-7 for azupyrene and 6-6-6-6 for pyrene. Some image features can be attributed to the different adsorption conformations of the two molecules: The rightmost ring of the pyrene molecule appears slightly elongated in the horizontal direction and contains a bright vertical feature (marked by red arrow in Fig. 3b). These features are presumably caused by tip-induced movements of the molecule between two different adsorption positions that occur during scanning. In the constant-height AFM image of azupyrene (Fig. 3a), the C and H atoms at the periphery appear brighter than atoms in the center of the molecule. This is caused by the bowl-shaped adsorption conformation of azupyrene on Cu(111) (see DFT results below). Therefore, the outer atoms are closer to the CO tip, which leads to their brighter appearance in the constant-height AFM images.²¹⁻²²

The adsorption topography of the molecules was obtained by three-dimensional frequency shift mapping (see Supplementary Fig. 3 for details).²³⁻²⁴ The reconstructed topographical information for the two molecules is shown in Fig. 3c,d of the main text. Corresponding topography scanlines indicating the apparent adsorption distances of the molecules with respect to the Cu(111) surface

plane are depicted in Fig. 3e. The scanlines have been taken along the short and long molecular axes, respectively (see arrows in Fig. 3c,d). Note that the topography values correspond to apparent adsorption distances, since these values are deduced from the interactions between the CO tip and the sample, which may be different for the different molecules (Supplementary Fig. 4). In other words, a different relative composition of the individual force contributions (Pauli repulsion, electrostatics, van der Waals) influences the apparent adsorption distance as measured by AFM.

In agreement with a study by Schuler et al.¹⁸ the measured adsorption distances are somewhat smaller than the calculated ones. This effect is particularly strong for reactive molecular species, such as radicals (see Ref. 18) or in our case azupyrene.

2.2 Supplementary TPD Discussion

The TPD traces shown in Fig. 4a of the main manuscript contain additional qualitative information, which will be discussed in the following. The TPD trace for initial monolayer coverage of azupyrene, which corresponds to the desorption of the upper 0.47 ML that can desorb, ranges from 330 to 650 K and is broader than that of pyrene (290 to 520 K). The peak at 400 K in the TPD spectrum of azupyrene is probably a decompression peak due to a phase transition in the molecular layer.

The broadening of the monolayer TPD traces reveals substantial intermolecular repulsion, which is attributed to dipole-dipole interactions between vertical adsorption dipoles. These dipoles are mainly caused by rearrangement of electron density at the metal surface due to Pauli repulsion induced by the electrons of the molecule (Pauli pushback effect).²⁵ The more pronounced broadening in the azupyrene case indicates stronger repulsion and thus larger adsorption dipoles, compared to the pyrene case, providing additional evidence for the increased interaction of azupyrene with the copper surface. Note that the observed desorption above a certain coverage also results from intermolecular repulsion: While isolated azupyrene molecules bind too strongly to the surface to desorb, lateral repulsion weakens the adsorbate-substrate bond with increasing coverage until desorption becomes possible.

The quantitative analysis of the TPD spectra shown in Fig. 4b of the main text was performed using two different approaches, the inverted Polanyi-Wigner equation approach (IPW, “Method 1” in Fig. 4b)²⁶ and an Arrhenius analysis of the leading edge (LNR, “Method 2” in Fig. 4b).²⁷ Both IPW and LNR yield the coverage dependent desorption activation energies, which are plotted in Fig. 4b.

The desorption prefactors obtained by LNR were also used for the IPW analysis and, in the case of pyrene, confirmed by prefactors obtained via heating rate variation (HRV) for the low coverage peaks (see Supplementary Fig. 7).²⁷

2.3 Supplementary XPS Discussion

If the monolayers of both molecules are annealed to temperatures higher than 300 K, the resulting XPS spectra provide complementary information to the TPD results (see Supplementary Fig. 5). The C 1s intensity of pyrene drops quickly between 300 and 500 K and only a very small residual intensity remains on the surface. TPD shows in this case a broad monolayer desorption peak between 300 and 500 K. The residual C 1s intensity is most likely caused by beam damage as the remaining fraction gets higher if the sample is exposed to the X-ray radiation over a longer time. For azupyrene the C 1s intensity decreases more slowly from a temperature of 300 K to 600 K, after which the intensity stays constant at a coverage of 0.53 monolayers. This finding is also in agreement with the TPD results, which show desorption only up to 600 K and with an irregularly steep high temperature tail of the desorption peak (Fig. 4a of the main text).

2.4 Supplementary UPS Discussion

According to a model potential used in the literature, the surface state shift for pyrene of 0.1 eV (visible in the UP spectra in Fig. 4d of the main text) corresponds to an adsorption height of about 3.1 Å.²⁸ For azupyrene, the surface state is not visible, its shift is therefore greater than 0.4 eV, for which the model potential would imply an adsorption height of less than 2.9 Å. But as this model potential is not applicable for strongly bonded systems, the value of its prediction is limited.

Interaction of the molecules with a metal surface influences the work function (WF), which can be determined from the secondary electron cut-off of the UP spectra. While both molecules reduce the work function, the change is more negative for azupyrene (-1.18 eV) than for pyrene (-0.86 eV). The experimental WF changes measured by UPS are also in agreement with the values calculated by DFT, where azupyrene possesses a larger value (-1.07 eV) than pyrene (-0.95 eV). For both molecules, the work function change is caused by the Pauli-pushback effect,^{25, 29-31} which is known to dominate the work function change for similar molecules regardless whether they are physisorbed or chemisorbed.³²⁻³³ The Pauli-pushback effect is strongly dependent on the adsorption height, thus azupyrene showing a larger WF change is in line with its smaller adsorption height as measured by nc-AFM and calculated by DFT.

This WF change is related to the vertical adsorption dipoles, which are responsible for the intermolecular repulsion observed in TPD. Even as the net charge transfer is from the surface to the molecule (see Supplementary Tab. 1), the rearrangement of electron density by the Pauli-pushback effect leads to a net dipole with the opposite direction. The orientation of the dipole agrees with the negative WF change experimentally observed by UPS. The magnitude of the DFT calculated dipole moment is 2.57 D for azupyrene and 2.25 D for pyrene, in line with the larger WF change and the stronger intermolecular repulsion observed in TPD. Thus, the larger WF

change for azupyrene corresponds to the stronger dipole-dipole repulsion in the desorption energy and overall confirms the stronger bonding of the model defect.

2.5 Supplementary HOMA Discussion

The change in the electronic structure of azupyrene due to the adsorption can also be discussed within the concept of aromaticity. One of the most widely used models to quantify aromaticity is the harmonic oscillator model of aromaticity (HOMA).³⁴ This model is based on the molecular geometry and the deviation of each bond from the ideal aromatic bond. The model parameters R_{opt} (the ideal aromatic bond length) and α are chosen such that the benzene molecule (with six equally long bonds) has a HOMA value of 1, whereas the hypothetical Kekulé-like benzene (with three single and three double bonds) has a HOMA value of 0. For the HOMA values discussed below we used the bond lengths obtained from the DFT-optimized structures of our molecules both free and adsorbed on the surface. The model parameters ($R_{\text{opt}} = 1.398 \text{ \AA}$ and $\alpha = 362.1 \text{ \AA}^{-2}$) used to calculate the HOMA values were determined employing the free benzene molecule and *trans*-butadiene optimized with the same method as a reference.

For each molecule with more than one aromatic ring, it is possible to calculate different HOMA values, depending on which π -bonds are taken into account. One possibility is to use all π -bonds in the molecule, this will be denoted as overall HOMA value O . If only the perimeter π -bonds of the molecule are used, this is called the perimeter HOMA value P . In addition, the HOMA value R for each ring can be calculated separately. Fig. S9a shows all these HOMA values for azupyrene and pyrene in their gas phase structure as well as adsorbed on Cu(111). Furthermore, we introduced the Excess Perimeter Conjugation (*EPC*).^{33, 35-36} This parameter is calculated as $EPC = P - O$ and provides a convenient way to determine if the molecule shows annulenic character, i.e. the aromatic conjugation is predominantly on the perimeter of the molecule, or if the conjugation is distributed over the whole molecule equally (benzenoid character). A higher *EPC* value therefore shows a more annulenic-like conjugation in the molecule. It should be noted that both molecules have the formula of $\text{C}_{16}\text{H}_{10}$, form a 16 π -electron system and should according to Hückel's $4n$ rule therefore be anti-aromatic. However, this is not the case and both molecules are aromatic, which was proven by NMR.³⁶⁻³⁷ In the following we will discuss how the two molecules find a different way to avoid Hückel's rule and form stable aromatic systems.³⁶

The free pyrene molecule shows a small *EPC* value of 0.04 which shows that no annulenic conjugation is present. It can be noted however, that the conjugation is not located equally over the whole molecule. The two apical rings possess higher HOMA values than the two other rings and these rings with the smaller HOMA value have one especially short bond. Both facts indicate that the most fitting description of the pyrene molecule is a biphenyl doubly bridged by ethenediyl units (Fig. S9b). The two apical rings form Clar sextets ($2 \times 6 \pi$ -electrons) and the ethylene bridges

form isolated double bonds ($2 \times 2 \pi$ -electrons), thus no 16 π -electron system is formed. Because of the weak interaction with the surface this situation stays the same when pyrene is adsorbed on Cu(111).

The free azupyrene molecule shows a large *EPC* value of 0.37 and also a short central bond with elongated bonds connecting the central two carbon atoms to the perimeter. Here, both facts are in agreement with the description as a [14]annulene with a inserted C_2 bridge (Fig. S9b). This way the 16 π -electrons are divided in the 14 π -electrons on the perimeter and 2 π -electrons in the isolated central double bond, forming two Hückel compliant systems. The strong bond formed between azupyrene and the Cu(111) surface influences the conjugation pattern of the molecule as can be seen in the HOMA values and bond length pattern. The *EPC* values decreases from 0.37 to 0.17, the bond in the central ethenetetrayl (C_2) unit is elongated and the four connecting bonds are shortened, giving rise to higher HOMA values for each ring. In a way, the interaction with the surface introduces a new way to bypass Hückel's rule and the 16 π -electron overall conjugation is now at least partially realized.

2.6 Supplementary DFT Discussion

To achieve a meaningful comparison of the DFT-calculated adsorption energies with the experimental values extracted from TPD, some care has to be taken. First, we need to choose a comparable coverage for both systems, in our case the (4×4) superstructure on Cu(111) with 16 surface atoms per adsorbed molecules. For this superstructure, the DFT adsorption energies are -243 kJ/mol for azupyrene, compared to -206 kJ/mol for pyrene. Therefore, DFT is qualitatively in agreement with the higher adsorption energy of azupyrene compared to pyrene.

Secondly, to compare these integral adsorption energies from DFT with the differential experimental desorption energies, the latter must be integrated up to the coverage employed in the calculations. The integrated desorption energies corresponding to the (4×4) structures used in the DFT calculations are 209 kJ/mol for azupyrene and 132 kJ/mol for pyrene. For the conversion from differential desorption energies, the results obtained by the IPW method were approximated with a second order polynomial. This polynomial function was used to extrapolate into the experimentally not accessible coverage range from 0.53 to 1 ML.

The deviation between experiment and theory of 34 and 74 kJ/mol is quite large, but the D3 dispersion correction used in the DFT calculation is well known for overestimating adsorption energies.^{32, 38-39} It is also not surprising that the overestimation is worse for pyrene, as this problem is most pronounced for physisorbed systems.³²

2.7 Supplementary pEDA Discussion

Even as it is weaker bound than azupyrene, pyrene still shows (in theory and experiment) a quite large adsorption energy. But the magnitude of the adsorption energy is no clear proof of a covalent chemisorptive bond to the surface. Obviously, big molecules often have large desorption energies, as the individually small dispersive interactions between all parts of the molecule and the surface add up, even leading to non-reversible adsorption (e.g. tetrapyrroles on metal surfaces⁴⁰). However, in the following we will show that the bond between pyrene and the surface is still physisorptive, whereas azupyrene forms a chemisorptive bond to the surface.

The application of the periodic energy decomposition analysis (pEDA) yields insight in the adsorbate-substrate bond by dividing the adsorption energy in various physically meaningful contributions. For this analysis the system is divided into two fragments, one containing the molecule and the other the surface. The constituent terms of the adsorption energy are then generated from the wave functions of the relaxed fragments, the fragments in the adsorbate state and the relaxed adsorbate structure.¹⁵

The pEDA analysis was performed on the PBE-D3 level of theory, using the (4×4) structure for both molecules on the Cu(111) surface. The calculations were tested for convergence regarding the k-space and for consistency against the results from the plane wave calculations above (with adjusted parameters for better comparability) in terms of the total bond energies ΔE_{bond} . The values for the bond energy (Supplementary Tab. 3) from both approaches agree within a quite large error of around 29 and 27 kJ/mol (11 and 12 %), also the k-space convergence is rather slow for these systems (see Supplementary Tab. 5). Nevertheless, the bonding interpretation based on the pEDA results is not affected since the differences between the systems are very large and show a qualitatively different bonding situation.

The pEDA energy terms compiled in Supplementary Tab. S3 show striking differences in the surface chemical bond of azupyrene and pyrene.

The dispersion part of the interaction energy, $\Delta E_{\text{int}}(\text{disp}) = -275$ (AzPyr) and -232 kJ/mol (Pyr), is the major stabilizing contribution for both molecules to the total interaction energy, $\Delta E_{\text{int}} = -302$ (AzPyr) and -223 kJ/mol (Pyr). The electronic part of the interaction energy is much smaller than the dispersive part for azupyrene and even repulsive for pyrene, $\Delta E_{\text{int}}(\text{elec}) = -27$ (AzPyr) and $+9$ kJ/mol (Pyr). The small magnitude of the electronic interaction energy is the result of the compensation of its constituent terms. In these terms the vastly different bonding situation of each molecule is apparent, with large differences in the electrostatic interaction, $\Delta E_{\text{elstat}} = -1270$ (AzPyr) and -312 kJ/mol (Pyr), the orbital interaction, $\Delta E_{\text{orb}} = -998$ (AzPyr) vs. -234 kJ/mol (Pyr), as well as in the Pauli repulsion, $\Delta E_{\text{Pauli}} = +2241$ (AzPyr) vs. $+555$ kJ/mol (Pyr). For azupyrene all of these terms are by a factor of four larger than for pyrene, strongly indicating a strong chemical interaction. The slightly larger contribution of the orbital attraction term to the total electronic attraction, 44 (AzPyr) vs. 43 % (Pyr), also is an indication of a more covalent bond for azupyrene.

Only because the dispersion term is responsible for a large portion of the total interaction energy, the resulting bond is not necessarily dispersive in nature. A better way to describe the situation is in saying that the molecule gains energy during the adsorption both by attractive dispersive and electronic interactions. At some distance to the surface the Pauli repulsion can overcompensate both attractive forces and establish an equilibrium. The electronic interaction energy then includes both attraction and repulsion whereas the dispersive interaction energy only includes the (necessarily) attractive contribution of the semi-empirical van-der-Waals correction.

In addition to the magnitude of the sub-terms of the electronic interaction energy, the presence of a strong chemical bond in the case of azupyrene is also visible in the large positive preparation energies ΔE_{prep} of molecule and surface, which are caused by the considerable distortion of both molecule and surface in the adsorbate structure.

The preparation energies for pyrene are smaller and in case of the molecule even negative, which should be impossible regarding the definition of the preparation energy.¹⁵ This unexpected behavior is observed if the preparation energies are calculated by comparing the deformed molecule layer with the free molecule in the ground state. In this case the mutual attraction of molecules in neighboring cells leads to a decrease in energy of the deformed fragment and a negative preparation energy ($\Delta E_{\text{prep}}(\text{mol, in cell})$). By using the isolated deformed molecule as a reference point instead of the deformed molecule layer, this attraction can be avoided, yielding the correct positive preparation energy ($\Delta E_{\text{prep}}(\text{mol, free})$).

2.8 Discussion of the NOCV extension of the pEDA analysis

The pEDA method enables us to look even deeper into the chemical bond when the NOCV (natural orbitals for chemical valence) scheme is employed to further decompose the orbital interaction term ΔE_{orb} .^{16, 41} In this scheme the electron density difference $\Delta\rho$ between the intermediate and final state in the pEDA analysis can be expressed by a set of NOCVs that diagonalize the resulting density matrix. These NOCVs come in pairs with matching eigenvalues of $\pm v_i$. They can be discussed very instructively in the form of deformation densities $\Delta\rho_i$. Each deformation density shows the electron flow caused by the formation of the interaction between the corresponding pair of NOCVs and can be connected to the energy gained and the eigenvalue v_i (which is an indicator of the amount of charge being transferred).

As one fragment is a metal surface the situation is more complex than for molecular systems, with a large number of NOCV terms contributing to the orbital interaction. However, the principal interactions determining the bonding situation can be identified by few dominant contributions. The parameters of the six most important deformation densities are compiled for both molecules in Tab. S4. Also, the magnitude of the eigenvalues (indicative of charge transfer) and the corresponding energies are much smaller. This weaker interaction is obvious when the deformation

densities are directly compared to those of azupyrene, as done in Fig. S8. The deformation densities of pyrene can only be visualized using a much smaller isosurface value. This is in agreement with a purely physisorptive bond where all deformation densities should only show slight charge rearrangement in the fragments.

Azupyrene possesses substantially larger eigenvalues and energies for the all deformation densities than pyrene, already showing the qualitative difference in interaction. The shape of the first two deformation densities of azupyrene (Fig. S8) clearly shows the outlines of the molecular LUMO and LUMO+1 orbitals as space of electron accumulation. For pyrene, no deformation density with clear assignment to molecular orbital shapes could be found.

3. Supplementary Figures

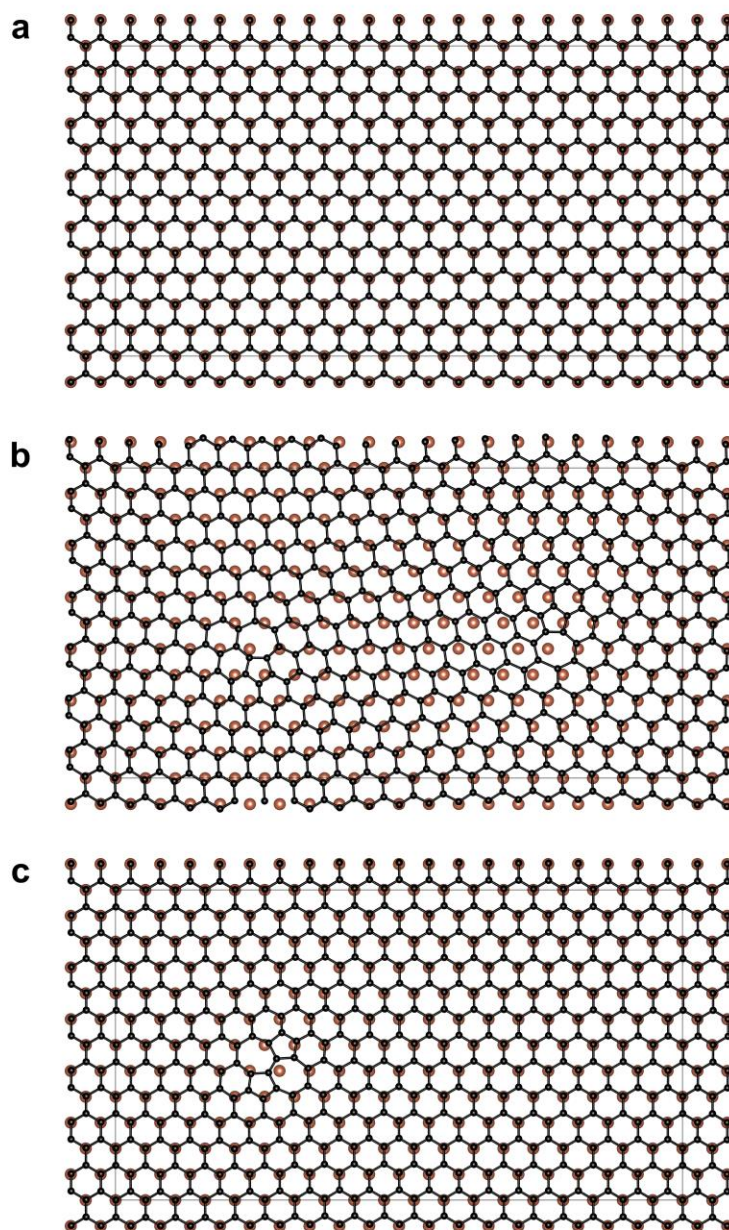


Figure S1. Complete unit cells used for the DFT calculations of the Graphene defects. Each unit cell contains 456 carbon atoms and a four-layer slab of the Cu(111) surface with 921 copper atoms. The structure is a commensurate ($6\sqrt{3} \times 19$) supercell of the Cu(111) surface, with the (1 \times 1) superstructure of graphene already used in literature.¹⁷ The adsorption site of the idealized graphene lattice is the *top-fcc* structure, found to be the most stable one in literature.²⁹ (a) ideal graphene structure. (b) two 5-7 defects embedded in the structure. (c) One Stone-Wales defect embedded in the structure. The introduction of two 5-7 defects is necessary to account for the disclination introduced by an isolated defect of this type.⁴²

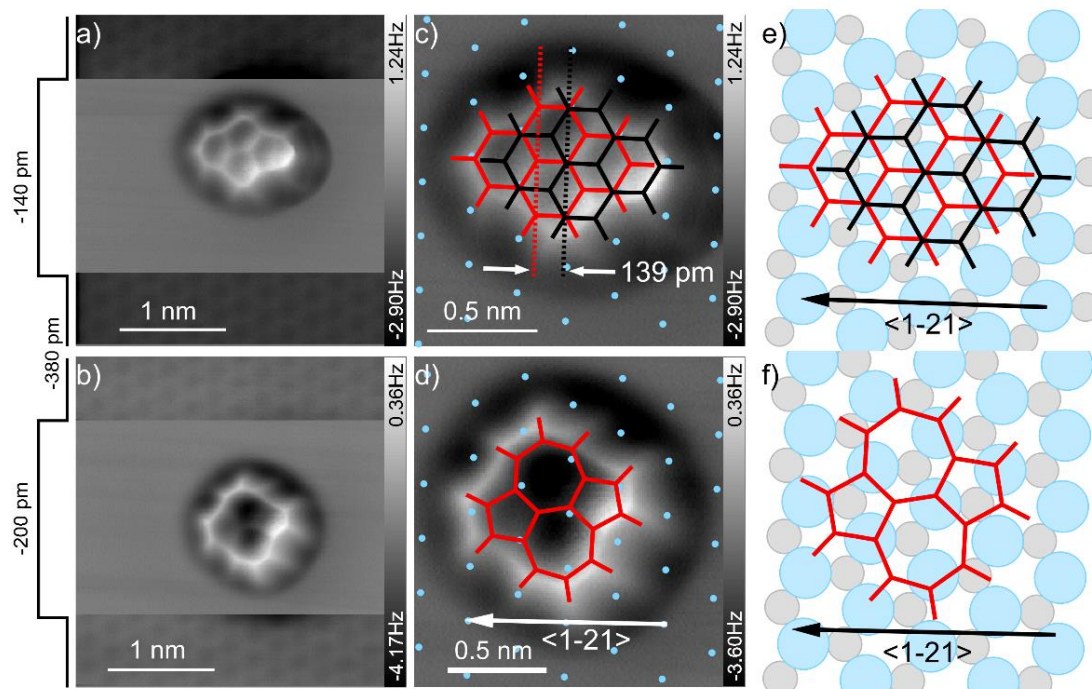


Figure S2. Determination of the adsorption positions of pyrene and azupyrene on Cu(111). (a,b) Constant-height frequency shift images at $z = -140$ pm (pyrene), $z = -200$ pm (azupyrene) and $z = -380$ pm (Cu surface) with respect to a tunneling set point of $U = 100$ mV and $I = 5$ pA. (c,d) Zoom-ins of (a,b) showing fitted positions of Cu(111) top sites (light blue) and fitted molecular structures (red and black). For pyrene two structures have been fitted, one to the left part of the molecule (red structure) and one to the rightmost ring that appears elongated in horizontal direction (black structure). (e,f) Sketches that indicate the measured adsorption positions with regard to the Cu(111) subsurface layer. The red and black molecular structures and the light blue circles (top sites) are identical to (c,d). The gray circles indicate the on-top positions of the Cu(111) subsurface atoms. These positions have been determined by an atomic resolution scan across a monoatomic step edge of the Cu(111) single crystal. The black arrows denote the crystallographic $\langle 1-21 \rangle$ directions.

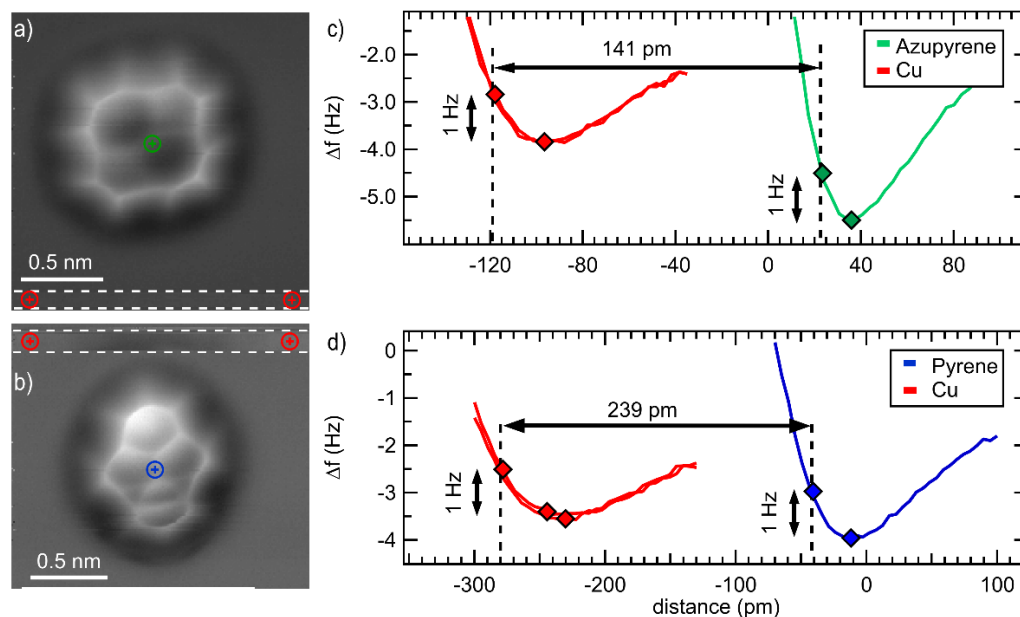


Figure S3. Determining the adsorption conformations and apparent adsorption distances of pyrene and azupyrene using 3D frequency shift mapping. (a,b) Slices of constant z taken from a 3D grid spectroscopy measurement of azupyrene and pyrene. Therefore, the frequency shift $\Delta f(z)$ has been measured in a box of $1.6 \times 1.6 \times 0.195 \text{ nm}^3$ at $160 \times 160 \times 30$ positions (azupyrene) and $1.9 \times 1.9 \times 0.17 \text{ nm}^3$ at $180 \times 180 \times 35$ positions (pyrene). The dashed white lines in a,b indicate regions where the starting point of the $\Delta f(z)$ curves was lowered to measure the interaction with the Cu surface. (c,d) Exemplary $\Delta f(z)$ spectroscopy curves that were measured over the centers of azupyrene (green line), pyrene (blue line), and the Cu(111) substrate (red lines). The positions of the curves are indicated in a,b by red, green, and blue markers. The “ $z = 0 \text{ pm}$ ” position in the two graphs corresponds to a tunneling setpoint of 100 mV and 100 pA for azupyrene (c) and 100 mV and 20 pA for pyrene (d). For determining the apparent adsorption distance of the molecules, first, for each curve the minimum of the $\Delta f(z)$ curve is determined (indicated by colored markers). The apparent adsorption distances are measured in the steep parts of the curves where the frequency shift has increased to a value of 1 Hz above the respective minima. As shown in the two graphs in (c,d) this results in an apparent adsorption distance of approx. 140 pm and 240 pm for the central parts of azupyrene and pyrene, respectively. This procedure was repeated at each pixel of the two images in (a,b) revealing the topography images that are presented in the manuscript in Fig. 3c,d.

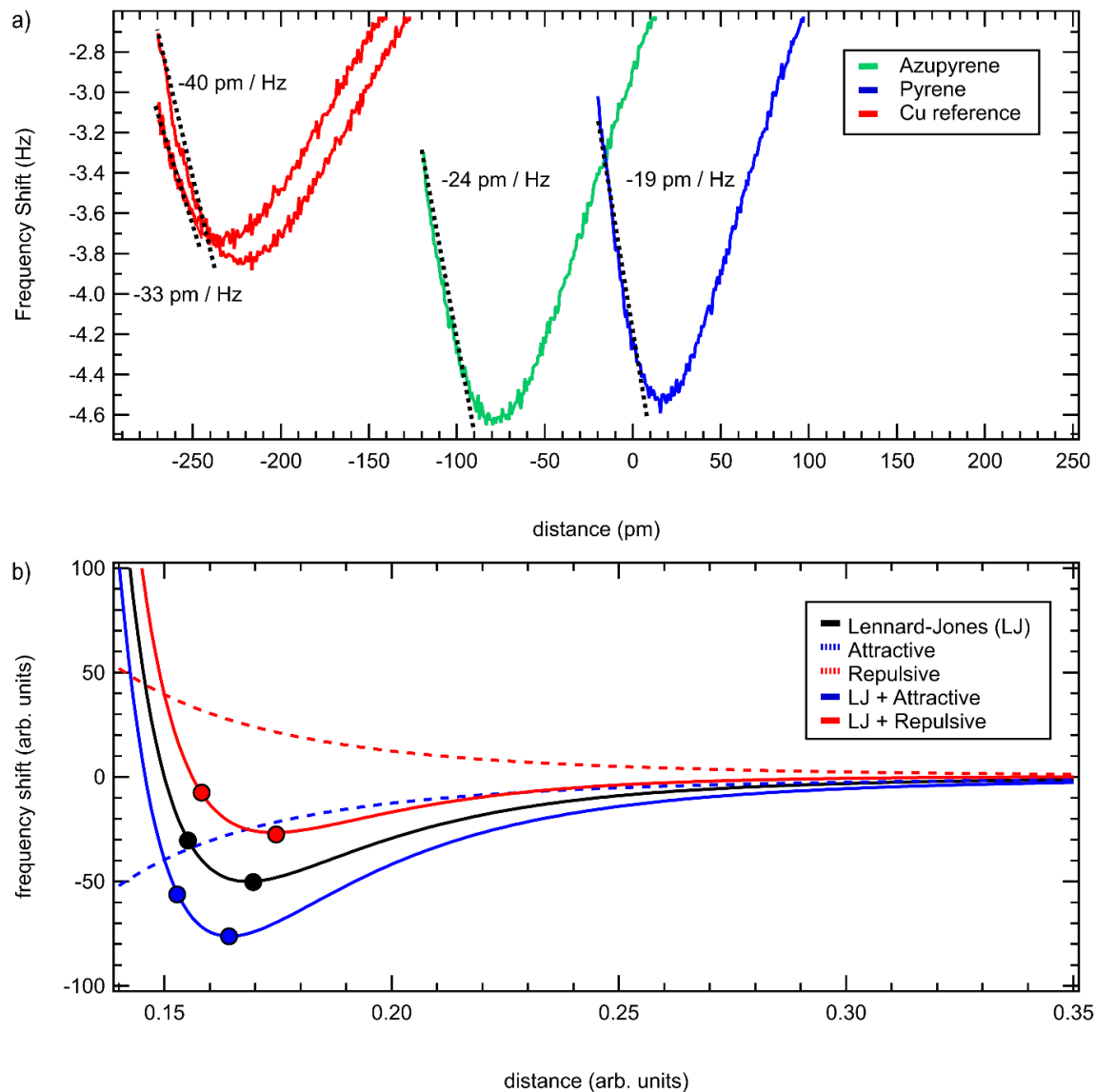


Figure S4. Apparent adsorption distance. (a) $\Delta f(z)$ curves measured over azupyrene (green), pyrene (blue), and Cu(111) (red). For each type of curve a different effective slope is observed in the part where the frequency increases (see dashed black lines). These different slopes lead to differences in the apparent adsorption distances. (b) Sketch that illustrates the effect of different tip-sample interaction contributions to the interaction potential. The black solid line represents a Lennard Jones potential between two atoms that is calculated by adding a relatively long range attractive potential ($\sim 1/z^6$) and a short range repulsive contribution ($\sim 1/z^{12}$). The red and blue dashed lines represent additional long range repulsive and attractive interaction contributions that could, for example, arise from different electrostatic interactions between the CO tip and the two molecules. These additional force contributions will obviously influence the measured apparent adsorption distances since it leads to a shift of the effective interaction curves in z-direction (see solid red and blue lines).

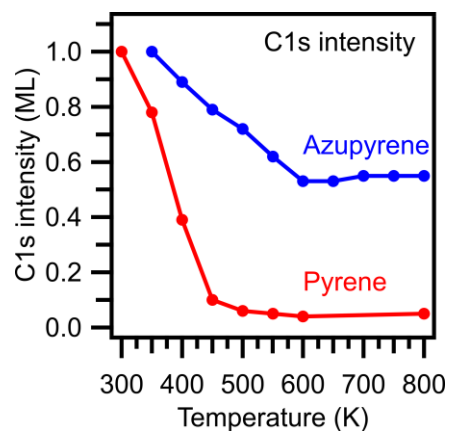


Figure S5. Temperature dependent XPS measurements. C 1s intensities of azupyrene (blue) and pyrene (red) in dependence of the temperature. While the intensity related to the pyrene coverage drops to zero at a temperature when the TPD indicates complete desorption, the azupyrene intensity does not drop if the sample temperature is increased above 650 K, indicating that 0.53 ML of azupyrene layer do not desorb but stick to the surface (and eventually decompose).

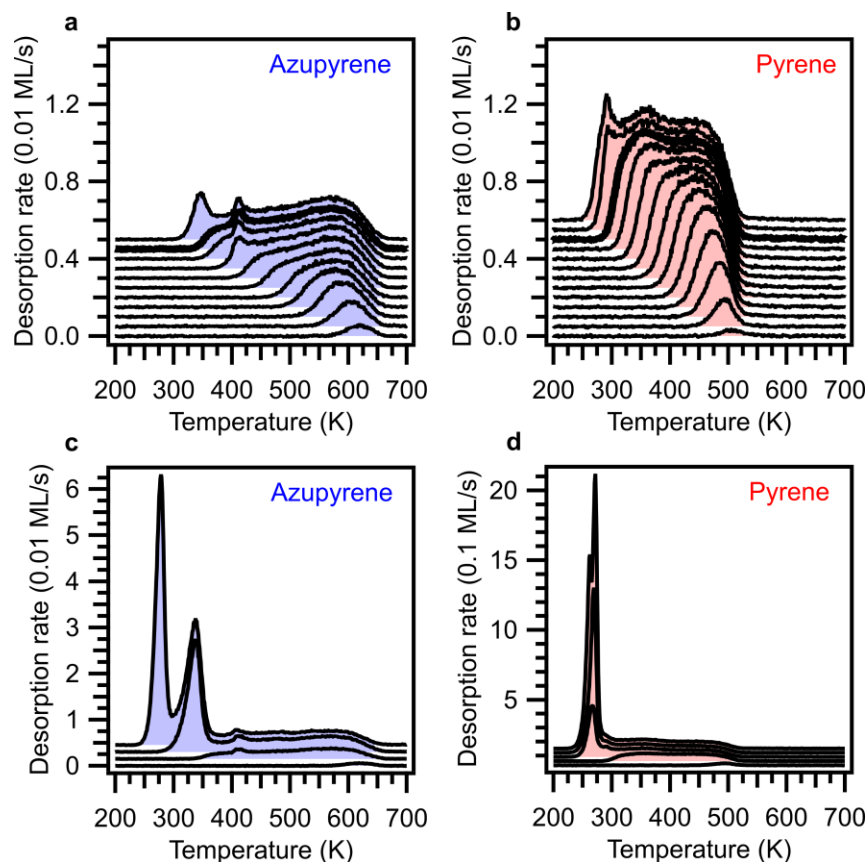


Figure S6. Extended TPD dataset. (a,b) TPD coverage series for pyrene (red) and azupyrene (blue) from submonolayer coverage to slightly over monolayer coverage, heating rate: 1 K/s, traces with a different initial coverage are shifted along the vertical axis. (c,d) coverage series for higher initial coverages showing the desorption of the bilayer and the beginning multilayer desorption.

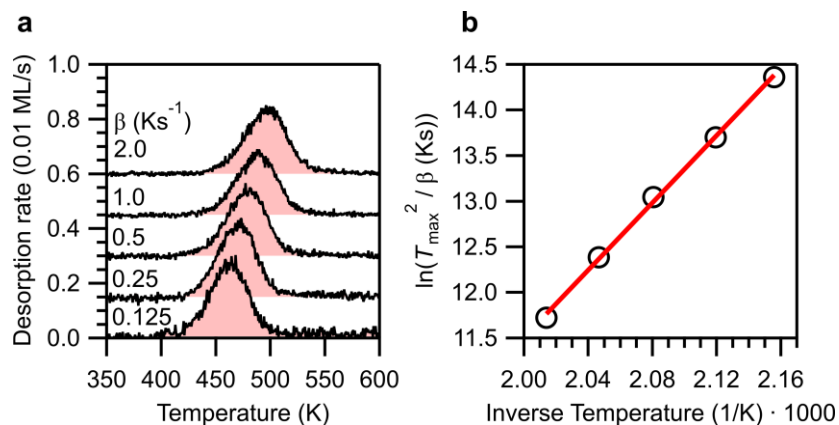


Figure S7. TPD heating rate variation analysis for pyrene. (a) TPD traces for an initial coverage of 0.1 ML measured with five different heating rates of 0.125 to 2.0 K/s, traces with a different heating rate shifted along the vertical axis. (b) Linear regression to determine the frequency factor.²⁷

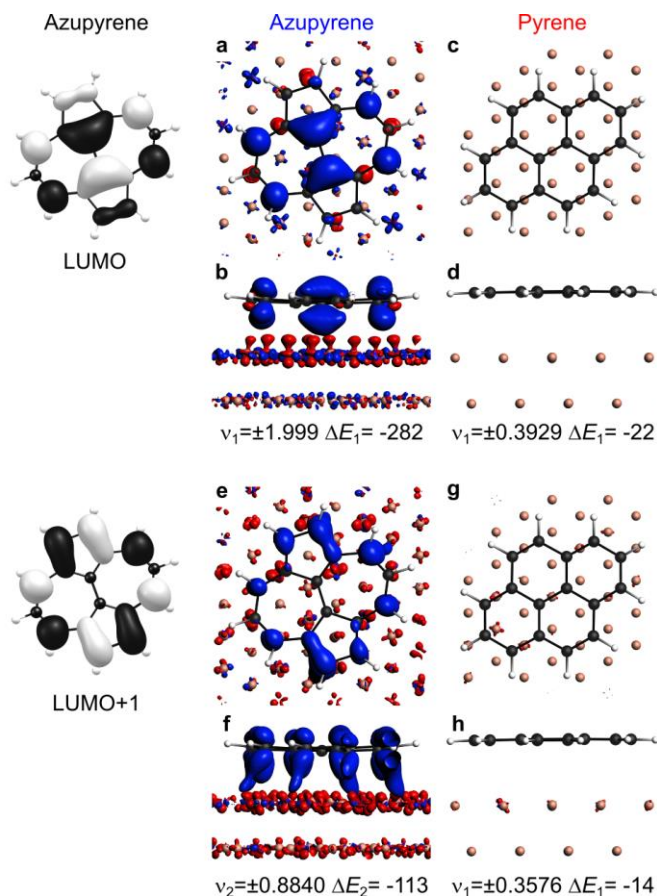


Figure S8. The pEDA analysis shows electron transfer from the Cu(111) surface into the unoccupied LUMO and LUMO+1 orbitals of azupyrene and no charge transfer for pyrene. Left, molecular LUMO and LUMO+1 orbitals of azupyrene. (a-h) Principal NOCV deformation densities ($\Delta\rho$) for azupyrene in comparison to pyrene, red denotes electron depletion, blue denotes electron accumulation. (a-d) $\Delta\rho_1$, isosurface value: $0.005 \text{ e}^-/\text{\AA}^3$. For azupyrene $\Delta\rho_1$ shows the electron transfer from the surface in the LUMO of the molecule, for pyrene it contains only minor rearrangement not visible at this isosurface value. (e-h) $\Delta\rho_2$, isosurface value: $0.001 \text{ e}^-/\text{\AA}^3$. For azupyrene $\Delta\rho_2$ shows electron transfer from the surface to the LUMO+1 of the molecule, for pyrene it again contains only minor charge rearrangements. All eigenvalues v_i in e and all energies in kJ/mol.

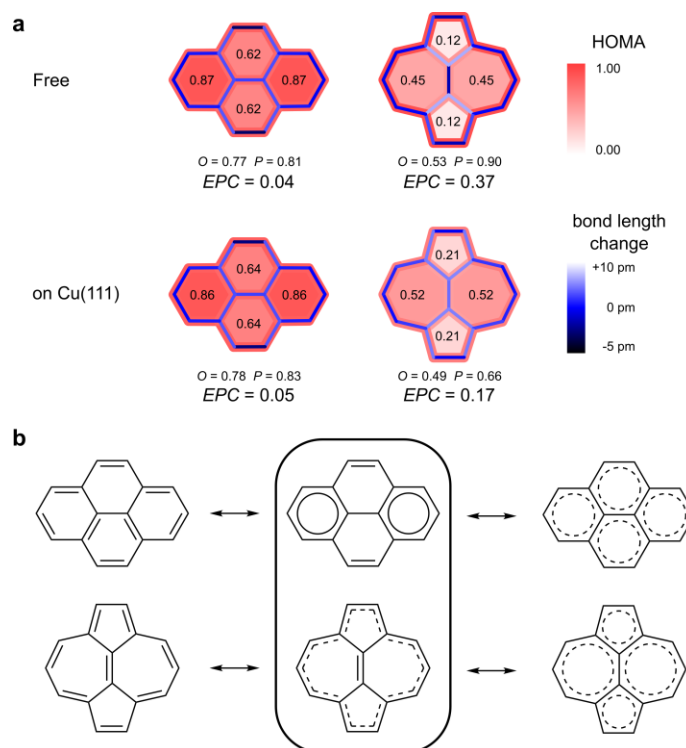


Figure S9. HOMA analysis for the azupyrene and pyrene molecules, each in its gas phase structure and the adsorbate structure on Cu(111). The red color scheme in (a) shows the HOMA value. The filling of each ring is colored in its respective HOMA value (R), the peripheral bonds are colored according to the peripheral HOMA value (P) and the bridging bonds are colored according to the overall HOMA value (O). All bonds are additionally colored with a blue color scheme according to the bond length change in respect to the ideal aromatic bond. The values for the gas phase structures have already been published in previous work.³⁶ (b) Comparison of different conjugation possibilities for azupyrene and pyrene. For pyrene the structure of the doubly ethenediyl bridged biphenyl with two Clar sextets is supported by the HOMA values, EPC s and bond lengths. The free azupyrene is best described with annulene-like conjugation, when adsorbed on Cu(111) the conjugation is more delocalized over the whole molecule. The structures at the right describe how overall (benzenoid) conjugation would be expressed.

4. Supplementary Tables

Table S1. Graphene defects induce localized charge transfer at the metal interface, similar to the molecules modelling the defects. The charge transfer was calculated by integrating the molecular projected DOS up to E_F , by Bader's atoms in molecules method,⁴³ by Hirshfeld's charge analysis,⁴⁴ and by an iterated Hirshfeld charge analysis scheme.⁴⁵⁻⁴⁷ The charge transfer for the graphene systems was calculated as the sum over the partial charges for the local group of atoms constituting the defect and their immediate neighbors (i.e., 42 atoms for the SW defect and 32 for the 5-7 defect). The charge transfer for the molecular systems pyrene (Pyr), azupyrene (AzPyr), and azulene (Az) was calculated both at equilibrium adsorption height, and with the molecule placed at the (larger) adsorption height of the graphene layer (denoted as @gr).

	ideal graphene	SW defect	5-7 defect	Pyr	Pyr @gr	AzPyr	AzPyr @gr	Az	Az @gr
q_{DOS}	-	-	-	-0.08	-	-1.40	-	-1.39	-
q_{AIM}	-	-	-	+0.02	-	-0.67	-	-0.49	-
q_H	+0.08	-0.10	-0.15	-0.04	+0.07	-0.31	-0.02	-0.25	-0.04
q_{H-I}	+0.06	-0.15	-0.20	-0.19	-0.04	-0.66	-0.15	-0.60	-0.15
All charges in e, a negative sign means electron density is transferred from the substrate to the graphene layer or molecule.									

Table S2. Localization of the charge transfer for the graphene defects. The charge transfer was again calculated by the iterated Hirshfeld charge analysis scheme.⁴⁵⁻⁴⁷ Here, we show that the charge transfer is indeed localized to the defect site. Towards this aim, we calculated the charge transfer as sum over the partial charges for different local groups of atoms around the defect site and for the whole layer with 456 carbon atoms. The local groups represent (1) the carbon atoms directly involved in the defect (16 atoms for the SW defect and 10 for the 5-7 defect), (2) those atoms and their immediate neighbors (42/32 atoms), and (3) those atoms and their neighbors (76/66 atoms). The charge transfer is given normalized per area (in e/nm^2).

	Whole layer	76/66 atoms	42/32 atoms	16/10 atoms
Ideal graphene	+0.05	+0.05	+0.05	+0.05
SW defect	-0.02	-0.08	-0.13	-0.31
5-7 defect	-0.01	-0.14	-0.23	-0.60
All charges in e/nm^2 , a negative sign means electron density is transferred from the substrate to the graphene layer.				

Table S3. pEDA results for azupyrene and pyrene on Cu(111), all energy values in kJ/mol.

	azupyrene	pyrene
ΔE_{int}	-302	-223
$\Delta E_{\text{int}}(\text{disp})$	-275	-232
$\Delta E_{\text{int}}(\text{elec})$	-27	+9
ΔE_{Pauli}	+2241	+555
$\Delta E_{\text{elstat}}^{\text{a}}$	-1270 (56 %)	-312 (57 %)
$\Delta E_{\text{orb}}^{\text{a}}$	-998 (44 %)	-232 (43 %)
$\Delta E_{\text{orb}}(\text{surf} \rightarrow \text{LUMO})$	-282	-
$\Delta E_{\text{orb}}(\text{surf} \rightarrow \text{LUMO}+1)$	-113	-
$\Delta E_{\text{prep}}(\text{mol, in cell})^{\text{b}}$	+18	-11
$\Delta E_{\text{prep}}(\text{mol, free})^{\text{c}}$	+31	+1
$\Delta E_{\text{prep}}(\text{surf})$	+12	+2
ΔE_{bond}	-271	-232
$\Delta E_{\text{bond}}(\text{PAW})$	-242	-205

^a Percentage values give the relative contributions to the sum of the attractive pEDA terms ΔE_{elstat} and ΔE_{orb}

^b referenced to the molecular fragment in the unit cell of the adsorbate structure

^c referenced to the isolated molecular fragment

Table S4. NOCV eigenvalues and corresponding orbital energy contributions for the most important deformation densities ($\Delta\rho_i$) resulting from an pEDA analysis of azupyrene and pyrene on Cu(111).

azupyrene			pyrene	
$\Delta\rho_i$	v_i / e	$\Delta E_{\text{orb},i} / \text{kJ/mol}$	v_i / e	$\Delta E_{\text{orb},i} / \text{kJ/mol}$
1	± 1.999	-282	± 0.3929	-22
2	± 0.8840	-113	± 0.3576	-14
3	± 0.6051	-58	± 0.3031	-20
4	± 0.5493	-39	± 0.2463	-12
5	± 0.5055	-37	± 0.2286	-11
6	± 0.4702	-36	± 0.2146	-13
$\Delta E_{\text{orb,rest}}$		-393	$\Delta E_{\text{orb,rest}}$	-110

The results of the periodic energy decomposition analysis were carefully checked for k-space convergence. Supplementary Tab. 5 shows the k-space convergence from k-grid 1×1 to 7×7 for both systems. As one can see the convergence is not especially good, but as the differences between the two systems are much greater, our discussion is still valid.

Table S5. k-space convergence for the pEDA calculations, basis set = TZ2P. Shown are the energies in kJ/mol and the deviation to the 7×7 value in percent.

ΔE_{int}	k-grid = 1×1		k-grid = 3×3		k-grid = 5×5		k-grid = 7×7
AzPyr/Cu	-284	-6%	-301	0%	-318	5%	-302
Pyr/Cu	-202	-10%	-213	-5%	-234	5%	-223
ΔE_{Pauli}	k-grid = 1×1		k-grid = 3×3		k-grid = 5×5		k-grid = 7×7
AzPyr/Cu	+2297	3%	+2257	1%	+2266	1%	+2241
Pyr/Cu	+572	3%	+555	0%	+565	2%	+555
ΔE_{elstat}	k-grid = 1×1		k-grid = 3×3		k-grid = 5×5		k-grid = 7×7
AzPyr/Cu	-1344	6%	-1308	3%	-1243	-2%	-1270
Pyr/Cu	-339	9%	-325	4%	-302	-3%	-312
ΔE_{orb}	k-grid = 1×1		k-grid = 3×3		k-grid = 5×5		k-grid = 7×7
AzPyr/Cu	-963	-4%	-975	-2%	-1066	7%	-998
Pyr/Cu	-203	-13%	-211	-10%	-266	13%	-234

Supplementary Tab. 6 directly compares the pEDA terms of the calculations performed with the 7×7 k-space grid to the values obtained by the NOCV calculation. All energy contributions show a good agreement with deviations of less than 6 % for azupyrene and less than 14 % for pyrene. The NOCV analysis, which can only be performed in the 1×1 grid, is therefore expected to give reasonable results and the energetic contributions $\Delta E_{\text{orb}}(\text{surf} \rightarrow \text{LUMO})$ and $\Delta E_{\text{orb}}(\text{surf} \rightarrow \text{LUMO}+1)$ assigned from the deformation densities of azupyrene are included in Tab. S3.

Table S6. Comparison of the pEDA contributions for k=7×7 calculations of the regular pEDA analysis and the k=1×1 (Γ -only) calculations performed for the NOCV extension.

	AzPyr/Cu		Pyr/Cu	
	k = 7×7	k=1×1	k=7×7	k=1×1
ΔE_{int}	-302	-284	-223	-202
$\Delta E_{\text{int}}(\text{disp})$	-275	-275	-232	-232
$\Delta E_{\text{int}}(\text{elec})$	-27	-9	+9	+30
ΔE_{Pauli}	+2241	+2297	+555	+572
ΔE_{elstat}	-1270	-1344	-312	-339
ΔE_{orb}	-998	-963	-234	-203

References

1. Kresse, G.; Hafner, J., Ab initio molecular dynamics for liquid metals. *Phys. Rev. B* **1993**, *47*, 558-561.
2. Kresse, G.; Hafner, J., Ab initio molecular-dynamics simulation of the liquid-metal-amorphous-semiconductor transition in germanium. *Phys. Rev. B* **1994**, *49*, 14251-14269.
3. Kresse, G.; Furthmüller, J., Efficient iterative schemes for ab initio total-energy calculations using a plane-wave basis set. *Phys. Rev. B* **1996**, *54*, 11169-11186.
4. Kresse, G.; Furthmüller, J., Efficiency of ab-initio total energy calculations for metals and semiconductors using a plane-wave basis set. *Comput. Mater. Sci.* **1996**, *6*, 15-50.
5. Perdew, J. P.; Burke, K.; Ernzerhof, M., Generalized Gradient Approximation Made Simple. *Phys. Rev. Lett.* **1996**, *77*, 3865-3868.
6. Grimme, S.; Antony, J.; Ehrlich, S.; Krieg, H., A consistent and accurate ab initio parametrization of density functional dispersion correction (DFT-D) for the 94 elements H-Pu. *J. Chem. Phys.* **2010**, *132*, 154104.
7. Becke, A. D.; Johnson, E. R., A density-functional model of the dispersion interaction. *J. Chem. Phys.* **2005**, *123*, 154101.
8. Blöchl, P. E., Projector augmented-wave method. *Phys. Rev. B* **1994**, *50*, 17953-17979.
9. Kresse, G.; Joubert, D., From ultrasoft pseudopotentials to the projector augmented-wave method. *Phys. Rev. B* **1999**, *59*, 1758-1775.
10. Clark, S. J.; Segall, M. D.; Pickard, C. J.; Hasnip, P. J.; Probert, M. I. J.; Refson, K.; Payne, M. C., First principles methods using CASTEP. *Z. Kristallogr. Cryst. Mater.* **2005**, *220*, 567–570.
11. Mizoguchi, T.; Tanaka, I.; Gao, S.-P.; Pickard, C. J., First-principles calculation of spectral features, chemical shift and absolute threshold of ELNES and XANES using a plane wave pseudopotential method. *J. Phys.: Condens. Matter* **2009**, *21*, 104204.
12. Triguero, L.; Pettersson, L. G. M.; Ågren, H., Calculations of near-edge x-ray-absorption spectra of gas-phase and chemisorbed molecules by means of density-functional and transition-potential theory. *Phys. Rev. B* **1998**, *58*, 8097-8110.
13. Klues, M.; Hermann, K.; Witte, G., Analysis of the near-edge X-ray-absorption fine-structure of anthracene: A combined theoretical and experimental study. *J. Chem. Phys.* **2014**, *140*, 014302.
14. Maurer, R. J.; Reuter, K., Excited-state potential-energy surfaces of metal-adsorbed organic molecules from linear expansion Δ -self-consistent field density-functional theory (Δ SCF-DFT). *J. Chem. Phys.* **2013**, *139*, 014708.
15. Raupach, M.; Tonner, R., A periodic energy decomposition analysis method for the investigation of chemical bonding in extended systems. *J. Chem. Phys.* **2015**, *142*, 194105.
16. Pecher, L.; Tonner, R., Deriving bonding concepts for molecules, surfaces, and solids with energy decomposition analysis for extended systems. *WIREs Comput Mol Sci.* **2019**, *9*, e1401.
17. Chanier, T.; Henrard, L., From carbon atom to graphene on Cu(111): an ab-initio study. *Eur. Phys. J. B* **2015**, *88*, 5.
18. Schuler, B.; Liu, W.; Tkatchenko, A.; Moll, N.; Meyer, G.; Mistry, A.; Fox, D.; Gross, L., Adsorption Geometry Determination of Single Molecules by Atomic Force Microscopy. *Phys. Rev. Lett.* **2013**, *111*, 106103.
19. Zhong, Q.; Ebeling, D.; Tschakert, J.; Gao, Y.; Bao, D.; Du, S.; Li, C.; Chi, L.; Schirmeisen, A., Symmetry breakdown of 4,4''-diamino-p-terphenyl on a Cu(111) surface by lattice mismatch. *Nat. Commun.* **2018**, *9*, 3277.
20. Ebeling, D.; Zhong, Q.; Schlöder, T.; Tschakert, J.; Henkel, P.; Ahles, S.; Chi, L.; Mollenhauer, D.; Wegner, H. A.; Schirmeisen, A., Adsorption Structure of Mono- and Diradicals on a Cu(111)

- Surface: Chemoselective Dehalogenation of 4-Bromo-3'-iodo-p-terphenyl. *ACS Nano* **2019**, *13*, 324-336.
21. Ebeling, D.; Šekutor, M.; Stieffermann, M.; Tschakert, J.; Dahl, J. E. P.; Carlson, R. M. K.; Schirmeisen, A.; Schreiner, P. R., London Dispersion Directs On-Surface Self-Assembly of [121]Tetramantane Molecules. *ACS Nano* **2017**, *11*, 9459-9466.
 22. Ebeling, D.; Šekutor, M.; Stieffermann, M.; Tschakert, J.; Dahl, J. E. P.; Carlson, R. M. K.; Schirmeisen, A.; Schreiner, P. R., Assigning the absolute configuration of single aliphatic molecules by visual inspection. *Nat. Commun.* **2018**, *9*, 2420.
 23. Hölscher, H.; Langkat, S. M.; Schwarz, A.; Wiesendanger, R., Measurement of three-dimensional force fields with atomic resolution using dynamic force spectroscopy. *Appl. Phys. Lett.* **2002**, *81*, 4428-4430.
 24. Schirmeisen, A.; Weiner, D.; Fuchs, H., Single-Atom Contact Mechanics: From Atomic Scale Energy Barrier to Mechanical Relaxation Hysteresis. *Phys. Rev. Lett.* **2006**, *97*, 136101.
 25. Witte, G.; Lukas, S.; Bagus, P. S.; Wöll, C., Vacuum level alignment at organic/metal junctions: "Cushion" effect and the interface dipole. *Appl. Phys. Lett.* **2005**, *87*, 263502.
 26. Tait, S. L.; Dohnálek, Z.; Campbell, C. T.; Kay, B. D., n-alkanes on MgO(100). I. Coverage-dependent desorption kinetics of n-butane. *J. Chem. Phys.* **2005**, *122*, 164707.
 27. Kachel, S. R.; Klein, B. P.; Morbec, J. M.; Schöniger, M.; Hutter, M.; Schmid, M.; Kratzer, P.; Meyer, B.; Tonner, R.; Gottfried, J. M., Chemisorption and Physisorption at the Metal/Organic Interface: Bond Energies of Naphthalene and Azulene on Coinage Metal Surfaces. *J. Phys. Chem. C* **2020**, *124*, 8257-8268.
 28. Armbrust, N.; Schiller, F.; Gütde, J.; Höfer, U., Model potential for the description of metal/organic interface states. *Scientific Reports* **2017**, *7*, 46561.
 29. Fernandez-Torrente, I.; Monturet, S.; Franke, K. J.; Fraxedas, J.; Lorente, N.; Pascual, J. I., Long-range repulsive interaction between molecules on a metal surface induced by charge transfer. *Phys. Rev. Lett.* **2007**, *99*, 176103.
 30. Lukas, S.; Vollmer, S.; Witte, G.; Wöll, C., Adsorption of acenes on flat and vicinal Cu(111) surfaces: Step induced formation of lateral order. *J. Chem. Phys.* **2001**, *114*, 10123-10130.
 31. Tomba, G.; Stengel, M.; Schneider, W. D.; Baldereschi, A.; De Vita, A., Supramolecular self-assembly driven by electrostatic repulsion: The 1D aggregation of rubrene pentagons on Au111. *ACS Nano* **2010**, *4*, 7545-51.
 32. Klein, B. P.; van der Heijden, N. J.; Kachel, S. R.; Franke, M.; Krug, C. K.; Greulich, K. K.; Ruppenthal, L.; Müller, P.; Rosenow, P.; Parhizkar, S.; Bocquet, F. C.; Schmid, M.; Hieringer, W.; Maurer, R. J.; Tonner, R.; Kumpf, C.; Swart, I.; Gottfried, J. M., Molecular Topology and the Surface Chemical Bond: Alternant Versus Nonalternant Aromatic Systems as Functional Structural Elements. *Phys. Rev. X* **2019**, *9*, 011030.
 33. Klein, B. P.; Morbec, J. M.; Franke, M.; Greulich, K. K.; Sachs, M.; Parhizkar, S.; Bocquet, F. C.; Schmid, M.; Hall, S. J.; Maurer, R. J.; Meyer, B.; Tonner, R.; Kumpf, C.; Kratzer, P.; Gottfried, J. M., Molecule-Metal Bond of Alternant versus Nonalternant Aromatic Systems on Coinage Metal Surfaces: Naphthalene versus Azulene on Ag(111) and Cu(111). *J. Phys. Chem. C* **2019**, *123*, 29219-29230.
 34. Kruszewski, J.; Krygowski, T. M., Definition of aromaticity basing on the harmonic oscillator model. *Tetrahedron Lett.* **1972**, *13*, 3839-3842.
 35. Klein, B. P.; Harman, S. E.; Ruppenthal, L.; Ruehl, G. M.; Hall, S. J.; Carey, S. J.; Herritsch, J.; Schmid, M.; Maurer, R. J.; Tonner, R.; Campbell, C. T.; Gottfried, J. M., Enhanced Bonding of Pentagon-Heptagon Defects in Graphene to Metal Surfaces: Insights from the Adsorption of Azulene and Naphthalene to Pt(111). *Chem. Mater.* **2020**, *32*, DOI: 10.1021/acs.chemmater.9b03744.

36. Klein, B. P.; Ruppenthal, L.; Hall, S. J.; Sattler, L. E.; Weber, S. M.; Herritsch, J.; Jaegermann, A.; Maurer, R. J.; Hilt, G.; Gottfried, M., Topology Effects in Molecular Organic Electronic Materials: Pyrene and Azupyrene. *ChemPhysChem* **2021**, *22*, 1065-1073.
37. Anderson, A. G.; MacDonald, A. A.; Montana, A. F., Dicyclopenta[ef,kl]heptalene (azupyrene). *J. Am. Chem. Soc.* **1968**, *90*, 2993-2994.
38. Maurer, R. J.; Ruiz, V. G.; Tkatchenko, A., Many-body dispersion effects in the binding of adsorbates on metal surfaces. *J. Chem. Phys.* **2015**, *143*, 102808.
39. Maurer, R. J.; Ruiz, V. G.; Camarillo-Cisneros, J.; Liu, W.; Ferri, N.; Reuter, K.; Tkatchenko, A., Adsorption structures and energetics of molecules on metal surfaces: Bridging experiment and theory. *Prog. Surf. Sci.* **2016**, *91*, 72-100.
40. Chen, M.; Röckert, M.; Xiao, J.; Drescher, H.-J.; Steinrück, H.-P.; Lytken, O.; Gottfried, J. M., Coordination Reactions and Layer Exchange Processes at a Buried Metal–Organic Interface. *J. Phys. Chem. C* **2014**, *118*, 8501-8507.
41. Mitoraj, M. P.; Michalak, A.; Ziegler, T., A Combined Charge and Energy Decomposition Scheme for Bond Analysis. *J. Chem. Theory Comput.* **2009**, *5*, 962-975.
42. Yazyev, O. V.; Louie, S. G., Topological defects in graphene: Dislocations and grain boundaries. *Phys. Rev. B* **2010**, *81*, 195420.
43. Bader, R. F. W., *Atoms in Molecules - A Quantum Theory*. Oxford University Press: Oxford, 1990.
44. Hirshfeld, F. L., Bonded-Atom Fragments for Describing Molecular Charge Densities. *Theor. Chim. Acta* **1977**, *44*, 129-138.
45. Bultinck, P.; Van Alsenoy, C.; Ayers, P. W.; Carbó-Dorca, R., Critical analysis and extension of the Hirshfeld atoms in molecules. *J. Chem. Phys.* **2007**, *126*, 144111.
46. Vanpoucke, D. E. P.; Bultinck, P.; Van Driessche, I., Extending Hirshfeld-I to bulk and periodic materials. *J. Comput. Chem.* **2013**, *34*, 405-417.
47. Vanpoucke, D. E. P.; Van Driessche, I.; Bultinck, P., Reply to ‘comment on “extending Hirshfeld-I to bulk and periodic materials”’. *J. Comput. Chem.* **2013**, *34*, 422-427.